Journal of Materials Chemistry C

Accepted Manuscript

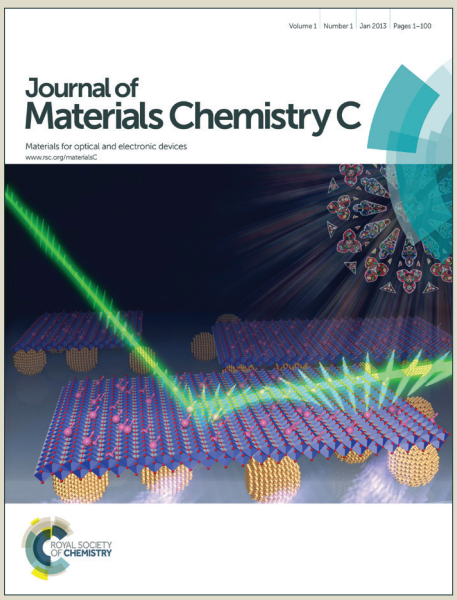

ROYAL SOCIETY OF CHEMISTRY

www.rsc.org/materialsC

Journal of Materials Chemistry C RSCPublishing

ARTICLE

Rubicene: A Molecular Fragment of C_{70} for Use in Organic Field-Effect Transistors†

Cite this: DOI: 10.1039/x0xx00000x

Received 00th January 2012,
Accepted 00th January 2012

DOI: 10.1039/x0xx00000x

www.rsc.org/

Hyunbok Lee,[a] Yue Zhang,[a] Lei Zhang,[a] Timothy Mirabito,[a] Edmund K. Burnett,[a] Stefan Trahan,[a] Ali Reza Mohebbi,[b] Stefan C. B. Mannsfeld,[c] Fred Wudl[b] and Alejandro L. Briseno*[a]

Rubicene, a molecular fragment of C_{70}, is a promising organic semiconductor material that displays excellent electronic characteristics for use in organic field-effect transistors (OFETs). Bottom-gate/bottom-contact polycrystalline thin-film OFETs using rubicene exhibit a saturation hole mobility of 0.20 $cm^2/V{\cdot}s$ and a current on/off ratio (I_{on}/I_{off}) of 1.0×10^4. In addition, the device performance can be improved with a mobility of 0.32 $cm^2/V{\cdot}s$ and I_{on}/I_{off} of 2.5×10^4 with pentafluorobenzenethiol (PFBT) self-assembled monolayer (SAM) treatment on Au electrodes. To characterize the interfacial electronic structure and morphology of rubicene on Au and PFBT/Au, ultraviolet photoelectron spectroscopy (UPS), theoretical calculation with density functional theory (DFT) and grazing incidence x-ray diffraction (GIXD) were performed. With PFBT SAM treatment, the hole injection barrier from Au to rubicene is significantly decreased from 1.15 to 0.48 eV due to the formation of a large interface dipole on Au that increased its work function from 4.33 to 5.67 eV. Furthermore, PFBT SAM treatment also induces an "edge-on" configuration of rubicene, which can lead to the increase in carrier mobility. These results indicate that rubicene can serve as a benchmark organic semiconductor for model charge transport studies and in various organic electronic devices.

Introduction

Molecular fragments of carbon nanotubes,[1-4] graphene,[5,6] and fullerenes[7,8] have garnered interest due to their unusual optical and electronic properties. These fragments are of particular interest as they serve as model systems for understanding electronic structure, chemical reactivity, and charge transport. Cyclopenta-fused polycyclic aromatic hydrocarbons (CP-PAHs), in particular, exhibit high electron affinities which are well suited for organic semiconductor applications due to the driving force to aromatize the cyclopentadiene by accepting an electron.[9,10] Recently, new CP-PAHs such as indenofluorenes,[11,12] emeraldicenes,[13,14] and cyclopenta[*hi*]aceantrylenes,[15] and even polymers have been synthesized and employed as electron-accepting and ambipolar materials for organic photovoltaics (OPVs) or OFETs.[16-18]

As a fragment of C_{70}, rubicene ($C_{26}H_{14}$) is another interesting CP-PAH. Compared to other fullerene derivatives, which have bowl like structures, rubicene has planar π-orbital surfaces that could provide increased intermolecular electronic coupling. Although rubicene has recently received interest as a potential material in electronic devices and its interface morphology on SiO_2 was recently reported,[19] no work has been published in any organic electronic devices. In this respect, we first determined the single crystal x-ray structure, followed by evaluation of the semiconductor properties of rubicene with the electrical measurements of polycrystalline thin-film OFETs. In addition, we further enhanced device performance with the introduction of pentafluorobenzenethiol (PFBT) self-assembled monolayer (SAM) treatment on Au electrodes. To characterize the interfacial electronic structure and morphology of the rubicene thin-film on Au and PFBT/Au, a comprehensive study using ultraviolet photoelectron spectroscopy (UPS), theoretical calculations via density functional theory (DFT) and grazing incidence x-ray diffraction (GIXD) was performed. In recent years, several studies on organic/PFBT SAM/electrode system have been reported.[20-24] Most studies were carried out for solution-processed organic layer on PFBT/electrodes and the high work function and microstructure formation were presented. However, the comprehensive investigation for device characterization, electronic structure and morphology using OFETs, UPS, DFT and GIXD is still lacking, especially for thermally evaporated organic layer on PFBT/electrodes. Therefore, this study enabled us to show the excellent charge transport properties of rubicene as well as clarify the origin of the enhanced device performance of rubicene OFETs with PFBT SAM treatment in detail.

Results and Discussion

X-Ray Single Crystal Structure

Figure 1 shows the chemical structure of C_{70} and the crystal structure of rubicene. In Figure 1a, it is shown that rubicene (red-colored) is a molecular fragment of C_{70} and has two cyclopentadienes which can accept an electron through aromatic 4n+2 stabilization.[15,25] The C_{2h} symmetric planar structure of rubicene from x-ray crystallography analysis is depicted with an ORTEP representation in Figure 1b. In Figure 1c and 1d, the molecular packing of rubicene is viewed down the crystallographic b-axis and c-axis, respectively. The compound crystallizes in a monoclinic $P2_1/n$ space group to form brilliant red needles with unit cell parameters of: a = 16.291 Å, b = 5.144 Å, c = 19.056 Å, α = 90.00°, β = 97.02°, γ = 90.00°. When viewed along the c-axis, the molecules are π-stacked in two nonequivalent stacks that are nearly perpendicular to each other (ca. 84°) due to the occurrence of C-H…π intermolecular contacts. The molecules within a given stack are tilted ca. 47° with respect to the stacking axis, causing the molecules to assume a "staircase" structure.[26,27]

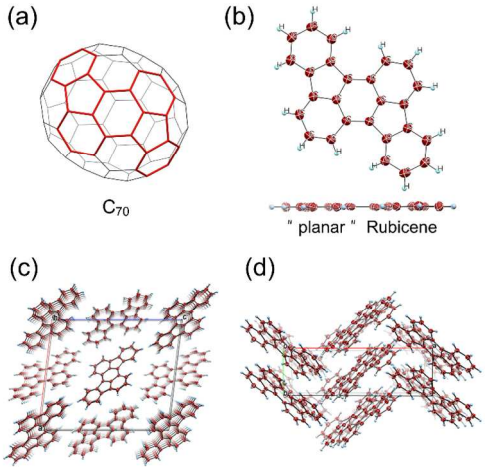

The distance between two adjacent parallel molecules is 3.38 Å, and these short contacts provide an efficient pathway for charge transport.[28]

Fig. 1 (a) The molecular structure of C_{70} showing the molecular fragment of rubicene ($C_{26}H_{14}$), (b) ORTEP representation of the crystal structure of rubicene as well as the planar view when rotated by 90°, (c) the molecular packing of rubicene as viewed down crystallographic b-axis, and (d) c-axis.

Rubicene OFETs Characteristics

Figure 2 shows the schematic configuration of bottom-gate/bottom-contact (BGBC) OFETs used in this study (a) and the measured electrical characteristics of the untreated (b and c) and PFBT SAM-treated rubicene OFETs (d and e). In Figure 2b, the output curves of the untreated rubicene OFETs show well-resolved saturation currents for several values of gate voltages (V_{GS}) from 0 V to -60 V with -10 V steps. Figure 2c shows the corresponding transfer characteristics in which both the log and the square-root of drain current (I_{DS}) were plotted as a function of V_{GS}. According to the linear and saturation field-effect mobility equations of $\mu_{lin} = (L/WC_iV_{DS})(\partial I_{DS}/\partial V_{GS})$ and $\mu_{sat} = (2L/WC_i)(\partial I_{DS}^{1/2}/\partial V_{GS})^2$, we determined hole mobilities of 0.05 $cm^2/V{\cdot}s$ in the linear region and 0.20 $cm^2/V{\cdot}s$ in the saturation region, and a current on/off ratio (I_{on}/I_{off}) of 1.0×10^4 at V_{DS} = -60 V. The device performance is improved with the PFBT SAM-treated Au electrodes. Hole mobilities are enhanced to 0.14 $cm^2/V{\cdot}s$ in the linear region and 0.32 $cm^2/V{\cdot}s$ in the saturation region, and I_{on}/I_{off} is also raised to 2.5×10^4 at V_{DS} = -60 V (Figure 2d and e). However, the threshold voltage (V_{th}) remains almost the same. In both the Au and PFBT SAM-treated Au OFETs, large differences between μ_{lin} and μ_{sat} are observed, which would be attributed to non-ignorable contact resistance between the Au electrodes and the rubicene channel. With PFBT SAM treatment, the ratio of μ_{sat} to μ_{lin} is decreased from 4.0 to 2.3, implying that PFBT SAM treatment could decrease the contact resistance. In both the Au and the PFBT SAM-treated Au, little hysteresis is observed during the forward and backward bias sweep, which might indicate minimum trapped carrier (we remark the measurements were carried out with the default settings of a Keithley 4200-SCS analyzer and the dynamic instability of charge transport is ignored[29]). The measured electrical characteristics of rubicene OFETs from more than six devices are summarized in Table 1. The dependence of mobility on V_{DS} and V_{GS} is also plotted in Figure S1 of ESI†.

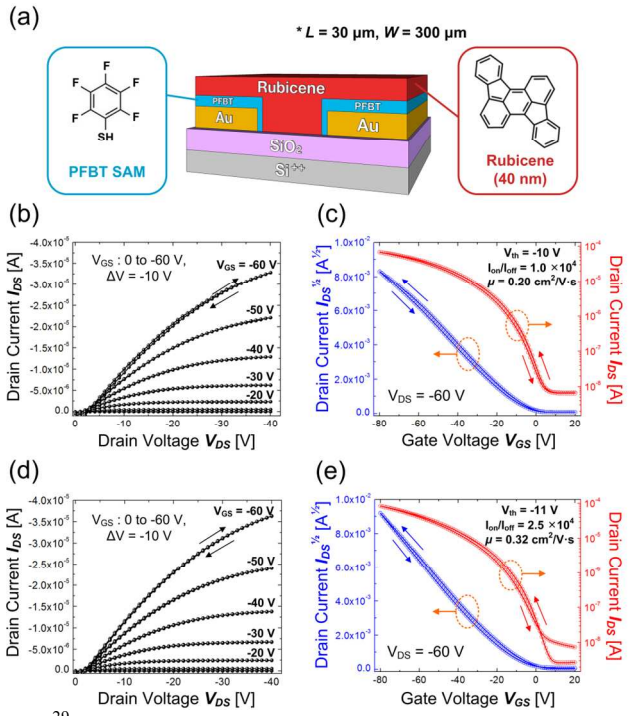

Fig. 2 (a) Schematic configuration of BGBC OFETs (channel length and width L = 30 μm, W = 300 μm and the thickness of a SiO_2 dielectric layer (C_i = 10 nF/cm^2) = 300 nm) and output and transfer/square root of current characteristics of the untreated [(b) and (c)] and PFBT SAM-treated rubicene OFETs [(d) and (e)], respectively.

Device	μ_{lin} (cm^2/Vs)	μ_{sat} (cm^2/Vs)	I_{on}/I_{off}	V_{th} (V)
Untreated Au	0.05 ± 0.03	0.20 ± 0.04	1.0×10^4	-10
PFBT-Au	0.14 ± 0.07	0.32 ± 0.04	2.5×10^4	-11

Table 1. The field-effect mobilities in the linear and saturation regime (μ_{lin} and μ_{sat}), current on/off ratios (I_{on}/I_{off}) and threshold voltage (V_{th}) of rubicene OFETs for comparison between the untreated Au and PFBT SAM-treated Au. All device characteristics were determined from more than six devices.

Theoretical Electronic Characteristics of Rubicene

To understand the origin of the high hole mobility and the enhanced device performance with PFBT SAM treatment in rubicene OFETs, the electronic structure and the morphology of rubicene on Au or PFBT/Au surfaces were investigated. Figure

3a and 3b show the wave functions of the lowest unoccupied molecular orbital (LUMO) and highest occupied molecular orbital (HOMO) of rubicene from DFT calculation. Although this theoretical calculation was carried out on a single molecule of rubicene, it approximates the electronic characteristics of its molecular solid film well due to the weak intermolecular interaction of organic semiconductors.[30] Especially, in polycrystalline organic thin-film, which exhibits weaker intermolecular interaction than single crystal, the single molecular structure dominantly contributes in the electronic properties of the solid-state. However, the calculated LUMO and HOMO values in a single molecule could slightly differ from the experimental values from its molecular solid film due to a lack of the screening effect.[31] Therefore, a qualitative analysis would be more pertinent.

In the LUMO and HOMO, the wave functions are delocalized over the entire molecule and show that large planar π-orbital surfaces could give high intermolecular electronic coupling as previously suggested. The frontier energy levels of rubicene are highly electron withdrawing due to the cyclopentadienes. The calculated Kohn-Sham eigenvalues of the LUMO and HOMO levels are -2.54 and -5.29 eV and these values are located deeper than those of the conventional *p*-type semiconductors, such as tetracene (-2.09 and -4.87 eV), pentacene (-2.40 and -4.61 eV), *α*-sexithiophene (-2.20 and -4.79 eV) and rubrene (-2.09 and -4.69 eV), at the same calculation level.[32-34]

In comparison to other CP-PAH cyclopenta[*hi*]aceanthrylenes, the HOMO of rubicene is

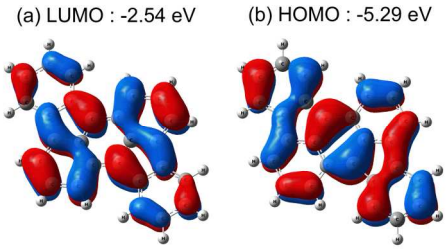

distributed over the entire anthracene backbone, whereas the HOMO of cyclopenta[*hi*]aceanthrylenes is relatively localized on the center of the anthracene backbone.[15] This largely delocalized HOMO of rubicene and its π-stacking (Figure 1c and 1d) could result in more efficient hole transport, and it corresponds well to the high hole mobility shown in OFET results.

Fig. 3 The wave functions and the Kohn-Sham eigenvalues of (a) LUMO, and (b) HOMO of rubicene from DFT calculation.

Energy Level Alignments of Rubicene from UPS

Figure 4a and 4b show the measured UPS spectra of the secondary electron cut-off (SEC) region and the HOMO region of Au, PFBT/Au, rubicene/Au and rubicene/PFBT/Au, respectively. For clear comparison, the spectra of the SEC region were normalized and Shirley-type background (contribution by inelastically scattered electrons) was removed from the measured HOMO region spectra. In the SEC region, the energetic difference between each onset implies the magnitude of the interface dipole (Δ). The SEC of Au is seen at 16.89 eV, which corresponds to a work function (Ψ) of 4.33 eV. This smaller work function than that of the clean Au (~5.2 eV) might originate from hydrocarbon contamination due to air-exposure.[35] These surface conditions are the same that would be used for OFETs. Upon PFBT SAM treatment on the Au substrate, the SEC is significantly shifted towards a lower binding energy by 1.34 eV. Therefore, the substrate's work function is conspicuously increased by the formation of the strong interface dipole with its positive pole (S atom) toward the Au surface.[20,36,37] As the rubicene layer is deposited, the SEC is shifted towards a higher binding energy by 0.12 eV on untreated Au, while by 0.61 eV on PFBT/Au. The HOMO level of rubicene on Au is seen at 1.15 eV, while on PFBT/Au it is seen at 0.48 eV below the Fermi level (E_F).

To estimate the LUMO level of rubicene, we measured the energy gap (E_g) with ultraviolet-visible absorption (Shimadzu, UV-3600) on a 100 nm-thick rubicene film on a glass substrate (Figure 4c). The spectral onset is seen at 600 nm, which corresponds to an energy gap of 2.07 eV. The absorption spectrum of this thin film is red-shifted compared to that of the solution-state of rubicene in toluene,[19] and the evaluated energy gap is more appropriate to estimate the LUMO level of rubicene used in solid-state electronic devices. This small energy gap would be also suitable for application in OPVs.

The energy level diagrams of rubicene/Au and rubicene/PFBT/Au are illustrated in Figures 4d and 4e, respectively. The work function of Au is 4.33 eV, therefore, the hole injection barrier (Φ_h) from Au to rubicene is measured to be around 1.15 eV. However, after PFBT SAM treatment, the hole injection barrier is dramatically decreased to 0.48 eV, although rubicene shows a relatively larger interface dipole on PFBT/Au (Δ = 0.61 eV) than on Au (Δ = 0.12 eV). Therefore, this reduced hole injection barrier would greatly contribute to the increased hole mobility of rubicene OFETs with PFBT SAM treatment. We note that somewhat smaller ionization energy of rubicene on Au (5.37 eV) than that on PFBT/Au (5.54 eV) might be attributed to the different molecular orientation (details on molecular orientation will be discussed in the following GIXD section).[24,38]

We additionally performed UPS measurements of rubicene on ITO substrates to ensure consistent ionization energy (IE) for rubicene (Figure S2 in ESI†). The evaluated ionization energy of rubicene on ITO is 5.57 eV. These ionization energies (5.5~5.6 eV) are similar to each other within experimental error. This higher ionization energy of rubicene than the conventional *p*-type organic semiconductors, such as pentacene (4.90 eV), *α*-sexithiophene (4.90 eV) and copper phthalocyanine (4.95 eV),[39-41] is experimentally ensured again and qualitatively corresponds to the above theoretically calculated HOMO value. Therefore, rubicene might be a candidate for ambipolar charge transport in OFETs or OPVs in terms of the frontier energy levels, and thus further study would be very promising. However, since the electron affinity of rubicene is ~3.4 eV, electrodes with a low work function should be selected for efficient electron injection. In addition, a top-contact geometry should be also chosen for *n*-type OFETs with device stability. This will be explored in due course.

Fig. 4 The measured UPS spectra of (a) the SEC region and (b) the HOMO

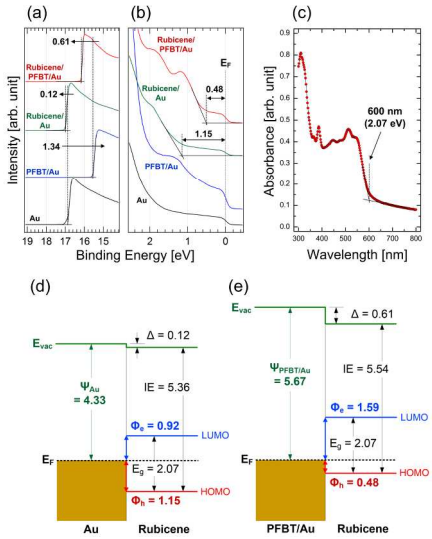

region of Au, PFBT/Au, rubicene/Au and rubicene/PFBT/Au and (c) ultraviolet-visible absorption spectrum of the rubicene film on a glass substrate and the energy level diagrams of (d) rubicene/Au and (e) rubicene/PFBT/Au.

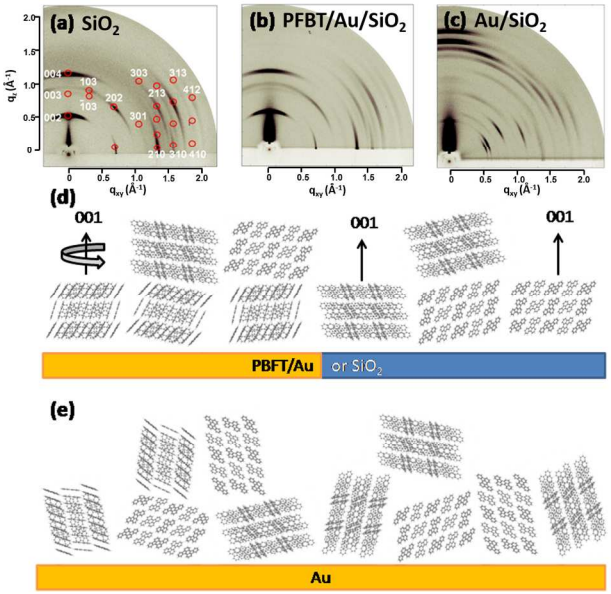

Fig. 5 GIXD images of rubicene thin films on different substrates: (a) SiO_2, (b) PFBT/Au/SiO_2 and (c) Au/SiO_2. On the SiO_2 and PFBT/Au/SiO_2 substrates, the rubicene GIXD patterns can be indexed as the bulk crystal structure with the (001) planes largely parallel to the substrate. On these surfaces the molecular packing is predominantly "edge-on" (d). On the bare Au surface however, the grain alignment is more random, but there is also a texture of more to a "face-on" oriented grains relative to the Au surface (e).

Morphology with GIXD

In polycrystalline thin films, the molecular packing is one of the most important factors determining the charge transport properties in the corresponding OFETs. The impact of the choice of substrate on the morphology of rubicene thin films was studied using GIXD. Figure 5a-c show 2D GIXD patterns of rubicene/SiO_2, rubicene/PFBT/Au/SiO_2 (PFBT SAM-treated Au substrate) and rubicene/Au/SiO_2 (untreated Au substrate) that illustrate the differences in rubicene crystal grains on the different surfaces in Figure 5d and 5e. On all three substrates, rubicene grows in the monoclinic bulk crystal structure (a = 16.291 Å, b = 5.145 Å, c = 19.056 Å, α = 90.00°, β = 97.02°, γ = 90.00°).

On the SiO_2 surface (Figure 5a), the diffraction pattern can be described by sets of Bragg rods of vertically aligned peaks. Despite a fair amount of arching in these peaks, which is indicative of orientational disorder in the grain orientation relative to the substrate surface, they can be indexed with the bulk structure oriented with its (001) plane parallel to the substrate surface (Figure 5d). The in-plane orientation of these grains is random, i.e. they form a 2D powder (indicated by rotation arrow in Figure 5d). With the (001) lattice planes being nearly parallel to the substrate, the molecules in the grains are packed in an edge-on configuration relative to the substrate.

On the PFBT SAM-treated Au substrates (Figure 5b and 5d), the diffraction pattern is nearly identical to that on SiO_2 with the exception of slightly more pronounced arching which means that the (001) planes are even less well aligned with the substrate planes than in the case of SiO_2.

Finally, on the bare Au substrate (Figure 5c and 5e), the rubicene diffraction pattern cannot be indexed by one specific crystal plane any longer and the grain orientation is far more random than in the SiO_2 or PFBT/Au cases. Still there is some texture present indicating more face-on grains than in the other two substrates. This orientation of grains is less favourable than the edge-on orientation which might partially explain the lower mobility on Au than on PFBT/Au as well as the larger contact resistance on Au than on PFBT/Au.[42]

Conclusions

In summary, rubicene polycrystalline thin-film OFETs show a hole mobility of 0.20 $cm^2/V{\cdot}s$ that can be further improved to 0.32 $cm^2/V{\cdot}s$ with the introduction of PFBT SAM treatment on Au electrodes. By UPS measurement, it is clearly shown that the hole injection barrier from Au to rubicene is significantly decreased with PFBT SAM treatment. In addition, GIXD measurement shows that PFBT SAM treatment induces an edge-on configuration of rubicene, which can lead to a higher hole mobility. Overall, the unique characteristics of rubicene, such as high hole mobilities, ambipolar valence energy levels, low energy gap, charge injection barrier and morphology on Au and PFBT/Au are presented in this study. Our investigation will expand the application possibility for use of rubicene in various efficient electronic devices as a *p*-type or an ambipolar semiconductor.

Experimental Section

Device fabrication and characterization

In a BGBC geometric configuration, polycrystalline thin-film OFETs were fabricated using heavily *p*-doped Si wafer with a SiO_2 dielectric layer (300 nm, C_i = 10 nF/cm^2). Lithographically patterned substrates of channel length (L) = 30 μm and width (W) = 300 μm were prepared by the sequential deposition of a Cr (5 nm) adhesion layer and Au (50 nm) source/drain electrodes with thermal evaporation under a high vacuum of ~1 × 10^{-6} mbar. The patterned substrates were ultrasonically cleaned with deionized water, acetone, and 2-propanol sequentially for 10 min each. The substrates were finally dried with high purity nitrogen gas prior to deposition of rubicene. For PFBT SAM treatment on Au electrodes, samples were immersed in a 10 mM PFBT (Sigma-Aldrich) solution in 2-propanol for 10 minutes, followed the recent reports.[43-45] The Wudl group synthesized rubicene and we later purchased it from Acros Organics (MW = 326.40, 98 %) and further purified by several recrystallization from hot toluene. For the active layer, a 40 nm thin film of rubicene was deposited onto the BGBC substrates with thermal evaporation. The electrical measurements of these rubicene-based *p*-channel OFETs were characterized using a Keithley 4200-SCS probe station unit in ambient conditions at room temperature.

Theoretical calculation with DFT

For theoretical investigation on the molecular electronic properties of rubicene, DFT calculation on single molecule of rubicene was performed. The Becke-3 parameters exchange and the Lee-Yang-Parr correlation (B3LYP) hybrid functional with

a 6-31G(d,p) basis set implemented in the Gaussian 09 package was used.[46-48] The molecular geometry was fully relaxed and the energetic minima was ensured by vibrational frequency analysis.

UPS measurement

UPS was carried out using an Omicron SPHERA hemispherical analyser and a He I (21.22 eV) excitation light source. To obtain the SEC, a sample bias of -3 V was applied in the normal emission geometry. The base pressure of the analysis chamber was 3×10^{-9} mbar. For the substrate, Au was thermally evaporated on the ITO-coated glass, and then a thin rubicene layer (6.0 nm) was deposited in a high vacuum chamber with the base pressure of 5×10^{-6} mbar at a rate of 0.1 nm/s. The thickness and deposition rates were monitored by a quartz crystal microbalance (QCM) calibrated by a surface profiler (KLA-Tencor, Alpha-Step IQ). To examine the effect of PFBT SAM treatment on the energy level alignment at the interface of rubicene/Au, we also prepared the rubicene thin film on the PFBT SAM-treated Au and conducted UPS measurement with the same procedure.

GIXD measurement

GIXD measurement was performed at beamline 11-3 Standord Synchrotron Light Source (SSRL) which operates at a fixed 12.7 keV energy. The grazing incidence angle was kept fixed at 0.12°. During the GIXD measurement, the samples were kept inside a He chamber to suppress the air scattering background, and a MAR345 image plate was used to collect the scattering signals. The peak indexing was done with house software that uses a Levenberg-Marquardt optimization to minimize the discrepancy between theoretical and experimentally measured peak positions.

Acknowledgements

A.L.B acknowledges support by the Office of Naval Research (N000141110636). UPS measurements were carried out as part of the Polymer-Based Materials for Harvesting Solar Energy laboratory, an Energy Frontier Research Center funded by the U.S. Department of Energy, Office of Basic Energy Sciences under Award Number DE-SC0001087. F.W and A. R. M thank the Department of Energy through Grant # DE-FG02-08ER46535. The authors thank Volodimyr V. Duzhko and Jayanta K. Baral for valuable discussion and support in the initial experimental setup.

Notes and references

[a] Department of Polymer Science and Engineering, University of Massachusetts Amherst, 120 Governors Drive, Amherst, MA 01003, USA. Email: abriseno@mail.pse.umass.edu; Fax: +1 4135450082; Phone: +1 4135771213

[b] Department of Chemistry and Biochemistry, University of California Santa Barbara, Santa Barbara, CA 93106, USA.

[c] Stanford Synchrotron Radiation Lightsource, SLAC National Accelerator Laboratory, Menlo Park, CA 94025, USA.

† Electronic Supplementary Information (ESI) available: Additional OFETs mobility plot, UPS and CIF. See DOI: 10.1039/b0 00000x/

1 J. Xia and R. Jasti, *Angew. Chem. Int. Ed.*, 2012, **51**, 2474-2476.
2 J. Xia, J. W. Bacon and R. Jasti, *Chem. Sci.*, 2012, **3**, 3018-3021.
3 T. Iwamoto, Y. Watanabe, Y. Sakamoto, T. Suzuki and S. Yamago, *J. Am. Chem. Soc.*, 2012, **133**, 8354-8361.
4 S. Yamago, Y. Watanabe and T. Iwamoto, *Angew. Chem. Int. Ed.*, 2010, **49**, 757-759.
5 L. Chen, Y. Hernandez, X. Feng and K. Müllen, *Angew. Chem. Int. Ed.*, 2012, **51**, 7640-7654.
6 L. Zhang, A. Fonari, Y. Zhang, G. Zhao, V. Coropceanu, W. Hu, S. Parkin, J.-L. Brédas and A. L. Briseno, *Chem.-Eur. J.*, in press (DOI: 10.1002/chem.201303308).
7 L. T. Scott, M. S. Bratcher and S. Hagen, *J. Am. Chem. Soc.*, 1997, **118**, 8743-8744.
8 B. D. Steinberg, E. A. Jackson, A. S. Filatov, A. Wakamiya, M. A. Petrukhina and L. T. Scott, *J. Am. Chem. Soc.*, 2009, **131**, 10537-10545.
9 M. Saito, M. Nakamura and T. Tajima, *Chem.-Eur. J.*, 2008, **14**, 6062-6068.
10 S.-H. Liao, J.-R. Shiu, S.-W. Liu, S.-J. Yeh, Y.-H. Chen, C.-T. Chen, T. J. Chow and C.-I. Wu, *J. Am. Chem. Soc.*, 2009, **131**, 763-777.
11 D. T. Chase, A. G. Fix, B. D. Rose, C. D. Weber, S. Nobusue, C. E. Stockwell, L. N. Zakharov, M. C. Lonergan and M. M. Haley, *Angew. Chem. Int. Ed.*, 2011, **50**, 11103-11106.
12 D. T. Chase, B. D. Rose, S. P. McClintock, L. N. Zakharov and M. M. Haley, *Angew. Chem. Int. Ed.*, 2011, **50**, 1127-1130.
13 A. R. Mohebbi and F. Wudl, *Chem.-Eur. J.*, 2011, **17**, 2642-2646.
14 A. R. Mohebbi, J. Yuen, J. Fan, C. Munoz, M. f. Wang, R. S. Chirazi, J. Seifter and F. Wudl, *Adv. Mater.*, 2011, **23**, 4644-4648.
15 J. D. Wood, J. Jellison, A. Finke, L. Wang and K. N. Plunkett, *J. Am. Chem. Soc.*, 2012, **134**, 15783-15789.
16 D. T. Chase, A. G. Fix, S. J. Kang, B. D. Rose, C. D. Weber, Y. Zhong, L. N. Zakharov, M. C. Lonergan, C. Nuckolls and M. M. Haley, *J. Am. Chem. Soc.*, 2012, **134**, 10349-10352.
17 H. Xia, D. Liu, X. Xu and Q. Miao, *Chem. Commun.*, 2012, **49**, 4301-4303.
18 J. Jellison, C.-H. Lee, X. Zhu, J. D. Wood and K. N. Plunkett, *Angew. Chem. Int. Ed.*, 2012, **51**, 12321-12324.
19 B. Scherwitzl, W. Lukesch, A. Hirzer, J. Albering, G. Leising, R. Resel and A. Winkler, *J. Phys. Chem. C*, 2013, **117**, 4115-4123.
20 Z. Jia, V. W. Lee, I. Kymissis, L. Floreano, A. Verdini, A. Cossaro and A. Morgante, *Phys. Rev. B*, 2010, **82**, 125457.
21 J. Smith, R. Hamilton, Y. Qi, A. Kahn, D. D. C. Bradley, M. Heeney, I. McCulloch and T. D. Anthopoulos, *Adv. Funct. Mater.*, 2010, **20**, 2330-2337.
22 R. Li, J. W. Ward, D.-M. Smilgies, M. M. Payne, J. E. Anthony, O. D. Jurchescu and A. Amassian, *Adv. Mater.*, 2012, **24**, 5553-5558.
23 C. H. Kim, H. Hlaing, F. Carta, Y. Bonnassieux, G. Horowitz and I. Kymissis, *ACS Appl. Mater. Interfaces*, 2013, **5**, 3716-3721.
24 J. W. Ward, M. A. Loth, R. J. Kline, M. Coll, C. Ocal, J. E. Anthony and O. D. Jurchescu, *J. Mater. Chem.*, 2012, **22**, 19047-19053.
25 H. Dang, M. Levitus and M. A. Garcia-Garibay, *J. Am. Chem. Soc.*, 2002, **124**, 136.
26 M. D. Curtis, J. Cao and J. W. Kampf, *J. Am. Chem. Soc.*, 2004, **126**, 4318-4328.
27 L. Zhang, L. Tan, W. Hu and Z. Wang, *J. Mater. Chem.*, 2009, **19**, 8216-8222.
28 V. Coropceanu, J. Cornil, D. A. d. S. Filho, Y. Olivier, R. Silbey and J.-L. Brédas, *Chem. Rev.*, 2007, **107**, 926-952.

29 Y. Chen, B. Lee, H. T. Yi, S. S. Lee, M. M. Payne, S. Pola, C.-H. Kuo, Y.-L. Loo, J. E. Anthony, Y. T. Tao and V. Podzorov, *Phys. Chem. Chem. Phys.*, 2012, **14**, 14142-14151.
30 D. R. T. Zahn, G. N. Gavrila and G. Salvan, *Chem. Rev.*, 2007, **107**, 1161-1232.
31 J. Sauther, J. Wüsten, S. Lach and C. Ziegler, *J. Chem. Phys.*, 2009, **131**, 034711.
32 D. A. d. S. Filho, E.-G. Kim and J. L. Brédas, *Adv. Mater.*, 2005, **17**, 1072-1076.
33 S. E. Koh, C. Risko, D. A. d. S. Filho, O. Kwon, A. Facchetti, J.-L. Brédas, T. J. Marks and M. A. Ratner, *Adv. Funct. Mater.*, 2008, **18**, 332.
34 V. T. T. Huong, T. B. Tai and M. T. Nguyen, *Phys. Chem. Chem. Phys.*, 2012, **14**, 14832-14841.
35 S. Rentenberger, A. Vollmer, E. Zojer, R. Schennach and N. Koch, *J. Appl. Phys.*, 2006, **100**, 053701.
36 H. Ishii, K. Sugiyama, E. Ito and K. Seki, *Adv. Mater.*, 1999, **11**, 605-625.
37 N. Koch, *ChemPhysChem*, 2007, **8**, 1438-1455.
38 S. Duhm, G. Heimel, I. Salzmann, H. Glowatzki, R. L. Johnson, A. Vollmer, J. P. Rabe and N. Koch, *Nat. Mater.*, 2008, **7**, 326-332.
39 I. Salzmann, G. Heimel, S. Duhm, M. Oehzelt, P. Pingel, B. M. George, A. Schnegg, K. Lips, R.-P. Blum, A. Vollmer and N. Koch, *Phys. Rev. Lett.*, 2012, **108**, 035502.
40 S. W. Cho, L. F. J. Piper, A. DeMasi, A. R. H. Preston, K. E. Smith, K. V. Chauhan, P. Sullivan, R. A. Hatton and T. S. Jones, *J. Phys. Chem. C*, 2010, **114**, 1928.
41 Y. Ge and J. E. Whitten, *Chem. Phys. Lett.*, 2007, **448**, 65-69.
42 W. H. Lee, J. Park, S. H. Sim, S. Lim, K. S. Kim, B. H. Hong and K. Cho, *J. Am. Chem. Soc.*, 2011, **133**, 4447-4454.
43 D. J. Gundlach, J. E. Royer, S. K. Park, S. Subramanian, O. D. Jurchescu, B. H. Hamadani, A. J. Moad, R. J. Kline, L. C. Teague, O. Kirillov, C. A. Richter, J. G. Kushmerick, L. J. Richter, S. R. Parkin, T. N. Jackson and J. E. Anthony, *Nat. Mater.*, 2008, **7**, 216-221.
44 R. Hamilton, J. Smith, S. Ogier, M. Heeney, J. E. Anthony, I. McCulloch, J. Veres, D. D. C. Bradley and T. D. Anthopoulos, *Adv. Mater.*, 2009, **21**, 1166-1171.
45 D.-K. Hwang, C. Fuentes-Hernandez, J. D. Berrigan, Y. Fang, J. Kim, W. J. Potscavage, H. Cheun, K. H. Sandhage and B. Kippelen, *J. Mater. Chem.*, 2012, **22**, 5531-5537.
46 A. D. Becke, *J. Chem. Phys.*, 1993, **98**, 5648.
47 C. Lee, W. Yang and R. G. Parr, *Phys. Rev. B*, 1988, **37**, 785-789.
48 M. J. Frisch, G. W. Trucks, H. B. Schlegel, G. E. Scuseria, M. A. Robb, J. R. Cheeseman, G. Scalmani, V. Barone, B. Mennucci, G. A. Petersson, H. Nakatsuji, M. Caricato, X. Li, H. P. Hratchian, A. F. Izmaylov, J. Bloino, G. Zheng, J. L. Sonnenberg, M. Hada, M. Ehara, K. Toyota, R. Fukuda, J. Hasegawa, M. Ishida, T. Nakajima, Y. Honda, O. Kitao, H. Nakai, T. Vreven, J. A. Montgomery, J. E. J. Peralta, F. Ogliaro, M. Bearpark, J. J. Heyd, E. Brothers, K. N. Kudin, V. N. Staroverov, R. Kobayashi, J. Normand, K. Raghavachari, A. Rendell, J. C. Burant, S. S. Iyengar, J. Tomasi, M. Cossi, N. Rega, J. M. Millam, M. Klene, J. E. Knox, J. B. Cross, V. Bakken, C. Adamo, J. Jaramillo, R. Gomperts, R. E. Stratmann, O. Yazyev, A. J. Austin, R. Cammi, C. Pomelli, J. W. Ochterski, R. L. Martin, K. Morokuma, V. G. Zakrzewski, G. A. Voth, P. Salvador, J. J. Dannenberg, S. Dapprich, A. D. Daniels, O. Farkas, J. B. Foresman, J. V. Ortiz, J. Cioslowski and D. J. Fox, Gaussian Inc., Wallingford CT, 2009.

